Published in final edited form as:
NMR Biomed. 2014 November ; 27(11): 1387–1396. doi:10.1002/nbm.3201.

Evaluation of Segmented 3D Acquisition Schemes for Whole-brain High-resolution Arterial Spin Labeling at 3T

Marta Vidorreta, MS[a], **Evelyne Balteau, PhD**[b], **Ze Wang, PhD**[c,d], **Enrico De Vita, PhD**[e,f], **María A. Pastor, MD, PhD**[a], **David L. Thomas, PhD**[e], **John A. Detre, MD**[d,g], and **María A. Fernández-Seara, PhD**[*,a]

[a]Neuroimaging Laboratory, CIMA, University of Navarra, Pamplona, Navarra, Spain

[b]Cyclotron Research Centre, University of Liège, Liège, Belgium

[c]Department of Psychiatry, University of Pennsylvania, Philadelphia, Pennsylvania, United States

[d]Department of Radiology, University of Pennsylvania, Philadelphia, Pennsylvania, United States

[e]Neuroradiological Academic Unit, Department of Brain Repair and Rehabilitation, UCL Institute of Neurology, London, United Kingdom

[f]Lysholm Department of Neuroradiology, National Hospital for Neurology and Neurosurgery, London, United Kingdom

[g]Department of Neurology, University of Pennsylvania, Philadelphia, Pennsylvania, United States

Abstract

Recent technical developments have significantly increased the SNR of arterial spin labeled (ASL) perfusion MRI. Despite this, typical ASL acquisitions still employ large voxel sizes. The purpose of this work was to implement and evaluate two ASL sequences optimized for whole-brain high-resolution perfusion imaging, combining pseudo-continuous ASL (pCASL), background suppression (BS) and 3D segmented readouts, with different in-plane k-space trajectories.

Identical labeling and BS pulses were implemented for both sequences. Two segmented 3D readout schemes with different in-plane trajectories were compared: Cartesian (3D GRASE), and spiral (3D RARE Stack-Of-Spirals). High-resolution perfusion images ($2\times2\times4$ mm^3) were acquired in fifteen young healthy volunteers with the two ASL sequences at 3T. The quality of the perfusion maps was evaluated in terms of SNR and gray-to-white matter contrast. Point-spread-function simulations were carried out to assess the impact of readout differences on the effective resolution.

The combination of pCASL, in-plane segmented 3D readouts and BS provided high-SNR high-resolution ASL perfusion images of the whole brain. Although both sequences produced excellent image quality, the 3D RARE Stack-Of-Spirals readout yielded higher temporal and spatial SNR than 3D GRASE (Spatial SNR = 8.5 ± 2.8 and 3.7 ± 1.4; Temporal SNR = 27.4 ± 12.5 and 15.6 ± 7.6, respectively) and decreased through-plane blurring due to its inherent oversampling of the

[*]CORRESPONDING AUTHOR María A. Fernández-Seara, Center for Applied Medical Research, University of Navarra, Pio XII, 55, 31008 Pamplona, Navarra, Spain, Telephone: +34 948 194700, Fax: +34 948 194715, mfseara@unav.es.

central k-space region, its reduced effective TE and shorter total readout time, at the expense of a slight increase in the effective in-plane voxel size.

Keywords

Perfusion imaging; arterial spin labeling; spiral imaging; high-resolution ASL; segmented readouts; cerebral blood flow

INTRODUCTION

Arterial Spin Labeled (ASL) perfusion MRI (1,2) utilizes magnetically labeled arterial blood water as an endogenous tracer, enabling non-invasive, quantitative measurements of tissue perfusion, in units of mL/min/100g of tissue. Although ASL MRI can potentially be carried out in any organ, the majority of studies to date have focused on measuring cerebral blood flow (CBF). ASL MRI has a broad range of applications in basic and clinical neuroscience (for a review, see (3)), including the evaluation of brain perfusion in disease states and its use as a means of monitoring brain function based on the tight coupling between regional CBF and neural activity (4).

The main limitation of ASL is its low intrinsic SNR: due to the T_1 decay of labeled blood from the labeling location to the tissue, and the small amount of labeled blood per tissue volume, only 1-2% of brain water can be magnetically labeled (5). Therefore, improving SNR of ASL MRI has been a major research goal, ever since its inception.

The proliferation of high field scanners has contributed to improving the sensitivity of ASL, both through increased raw image SNR and T_1 prolongation at higher field. Several additional technical developments have been introduced in order to further enhance the SNR of ASL. Pseudo-continuous ASL (pCASL) (6) has been demonstrated to provide higher perfusion signal compared to prior approaches while at the same time overcoming the technical hardware difficulties of continuous ASL (CASL). The use of 3D readout sequences (7-9) combined with background suppression (BS) schemes (10,11) that suppress the static tissue signal have also been proven to outperform 2D sequences in terms of SNR (12).

Despite this progress, most 3D ASL acquisitions (typically single-shot for some applications, such as stroke and functional activation assessment) still employ relatively large voxel sizes, especially in the slice direction, where blurring due to T_2 decay during the echo train severely limits the effective resolution. 3D multi-shot or segmented acquisitions have been proposed as an alternative to further increase the image SNR and/or resolution (6,13,14). Although segmented readouts require several RF excitations (or shots) to sample the complete k-space, and thus are ill-conditioned for dynamic ASL studies, in many cases ASL is simply used to quantify mean perfusion. For these applications, 3D segmented readouts offer several advantages, including reduced through-plane blurring and decreased susceptibility artifacts due to their shortened effective TE and readout time per shot.

The aim of this work was to implement and evaluate two ASL sequences optimized for whole-brain high-resolution perfusion imaging. Both sequences included an identical pCASL pulse and BS scheme combined with a segmented 3D readout. Two readout schemes with different in-plane trajectories were compared: Cartesian (3D GRASE (8,13,14)), and spiral (3D RARE Stack-Of-Spirals (6,11,15)). The same k-space trajectory in the slice direction was implemented for both sequences, to be able to specifically evaluate the effect of the different in-plane trajectories. Baseline perfusion measurements were acquired in a group of fifteen young healthy volunteers. The quality of the perfusion maps was assessed in terms of SNR and GM-WM contrast.

MATERIALS AND METHODS

Subjects

A total of 15 young healthy volunteers (8 females; mean age ± standard deviation (SD) = 25.5 ± 3.7 years) participated in the study, which was approved by the Ethics Committee of the University of Navarra. Written informed consent was signed by all participants prior to the scanning session.

Scanning protocol

The study was carried out on a 3-Tesla Siemens Trio (Siemens, Erlangen, Germany) using the standard 12-channel head array.

First, an anatomical T_1-weighed brain image was acquired with a MPRAGE sequence with the following imaging parameters: repetition time (TR) = 1620 ms, echo time (TE) = 3.09 ms, inversion time (TI) = 950 ms, flip angle = 15°, field-of-view (FOV) = 192×256×160 mm^3, resolution = 1 mm isotropic, matrix = 192×256×160, 160 axial slices, scan-time = 5.2 min. Next, a Time-Of-Flight (TOF) angiogram was acquired at the base of the brain with TR/TE = 22/3.86 ms, flip angle = 18°, 2 slabs of 40 nominal partitions acquired with 20% oversampling and slice partial Fourier (PF) = 6/8, phase PF = 6/8, FOV = 200×150×40 mm^3, resolution = 0.52×0.52×1 mm^3, matrix = 384×288×36, scan-time = 2.88 min. Finally, subjects underwent two resting perfusion scans, in which whole brain perfusion images were acquired using two high-resolution ASL sequences, in pseudo-randomized order: 3D RARE Stack-Of-Spirals and 3D GRASE. Both sequences were implemented with identical pseudo-continuous labeling and BS, and 3D segmented readouts. During each acquisition, 6 pairs of label-control images were obtained while the subjects were resting with their eyes closed, during a scan time of 400s, where each image was acquired over a 32s period, corresponding to the time needed for 8 RF excitations or shots (see below for acquisition details of the ASL readouts). Two additional control images without BS were acquired at the end of each scan for CBF quantification purposes.

The pCASL pulse consisted of 1520 selective RF pulses (Hanning window, B_1 average = 1.8 μT, duration = 500 μs, spacing = 500 μs, $G_{average}$ = 1 mT/m, $G_{maximum}/G_{average}$ = 8) with a labeling duration of 1527.6 ms and post-labeling delay (PLD) of 1500 ms. Identical gradient (G) waveforms were used for label and control acquisitions. The phase of each RF pulse was incremented by a constant amount to maintain coherence with the flowing spins

under the nonzero mean gradient. An additional phase-shift of 180° was applied to the control RF pulses.

The location of the inversion plane was determined for each subject based on the TOF angiograms, and maintained across sequences. In all cases, the inversion plane was located at the base of the cerebellum, with a mean offset of 85.5 ± 6.8 mm (range 80 - 104 mm) from the center of the FOV in the head-foot direction. The position was chosen so that the carotid and vertebral arteries were oriented as perpendicular to the inversion plane as possible (Fig. 1).

The same optimized BS scheme was added to both sequences. It comprised 4 presaturation pulses at the beginning of each TR, a slice-selective C-FOCI pulse (16) played immediately before labeling plus 2 non-selective hyperbolic secant pulses during the PLD, with timings optimized to suppress the static tissue signal to 10% of its equilibrium value: TI_1 = 1258.6 ms, TI_2 = 350 ms (12).

In-plane segmented acquisitions were implemented for both sequences, with 8 separate RF excitations (shots or segments). The number of segments was selected as the highest number that rendered a reduction in TE for both sequences. Increasing further the number of shots did not result in a decreased TE for 3D GRASE, because the TE was then limited by the duration of the interval between the 90° excitation RF pulse and the first 180° refocusing RF pulse.

During the 3D RARE Stack-Of-Spirals acquisition, every k_z plane was divided into 8 spiral interleaves, each of them being sampled after a single RF excitation (Fig. 2a). In the 3D GRASE acquisition, every k_z plane was divided into 8 segments in the in-plane phase-encoding (PE) direction (K_y), so that one in every 8 lines were sampled within each shot (Fig. 2b). Segmentation along the slice direction (K_z) was not implemented for either sequence.

The nominal resolution of both sequences was kept constant at 2×2×4 mm^3. The readout parameters were selected as follows:

- ***3D RARE Stack-Of-Spirals (***Fig. 3a***):*** TR = 4000 ms, effective TE (TE_{eff}) = 8.74 ms, excitation flip angle = 90°, refocusing flip angle = 180°, resolution = 2×2×4 mm^3, matrix = 128×128×27, 32 nominal partitions with 12.5% oversampling acquired using a centric encoding scheme and slice PF = 6/8 (27 acquired partitions), 8 interleaved spirals, maximum slew rate = 120 mT/(m·ms), maximum gradient amplitude = 36 mT/m, FOV = 256×256×128 mm^3, total readout time per shot = 349.8 ms.

  The spiral readout trajectory was generated numerically (17). The spiral calculation code was derived from Dr. Brian Hargreaves' code (http://mrsrl.stanford.edu/~brian/vdspiral/). Gradient raster time and ADC sampling time were 10 and 2.5 us, respectively (receiver bandwidth (BW) = 400 kHz). To avoid FOV aliasing artifacts, the Nyquist criterion was applied along the radial direction. The spiral trajectories were corrected prior to reconstruction by estimating the gradient time

delays (18). Spiral k-space data were then regridded to Cartesian coordinates using the standard regridding method with a Kaiser-Bessel window kernel (19), and a Voronoi diagram to correct non-uniform sampling density. The Fastest Fourier Transform in the West (FFTW) package (20) was used to transform the regridded data into image space.

- ***3D GRASE (***Fig. 3b***):*** TR/TE_{Eff} = 4055/16.96 ms, excitation flip angle = 90°, refocusing flip angle = 180°, resolution = 2×2×4 mm^3, matrix = 128×120×27, 32 nominal partitions in the slice-encoding direction with 12.5% oversampling acquired with a centric encoding scheme and slice PF = 6/8 (27 acquired partitions), BW = 2298 Hz/px, 2-fold oversampling in readout direction (BW = 588 kHz), FOV = 256×224×128 mm^3, in-plane phase-encoding direction = A-P, total readout time per shot = 466.4 ms.

  Gradient echo-shifting (21) was implemented to avoid amplitude discontinuities in the phase-encoding direction and ensure a smooth point spread function (PSF). This was accomplished by time-shifting the readout echo train of each k_z plane by a fixed amount that increased proportionally to the segment number.

Data processing

Data processing was conducted using SPM8 (Wellcome Trust Centre for Neuroimaging, University College London, UK) and custom scripts in Matlab (Mathworks, MA, USA). Raw label and control images were reconstructed offline, realigned and co-registered to the anatomical dataset, and then perfusion-weighted images were obtained by direct subtraction of the control and label images. CBF maps were computed from the perfusion-weighted images using the single-compartment model (22), where the control magnetization was computed from the average control images obtained without BS. A calibration factor of 0.72 was employed for absolute CBF quantification, as estimated in previous work (12). This takes into account the labeling efficiency as well as the efficiency of the BS pulses. A mean perfusion image and CBF map were obtained per sequence tested by averaging the 6 pairs acquired during each run.

Anatomical grey matter (GM), white matter (WM) and whole-brain masks were created for each subject, to extract mean GM, WM and whole-brain CBF values. All masks were obtained from the segmented tissue maps generated upon segmentation of individual MPRAGE images using the New Segment tool in SPM8. For the calculation of GM / WM mean CBF values only the inner voxels located in GM / WM in slices superior to the corpus callosum were included, to avoid partial volume effects (23) and possible susceptibility related artifacts found in ventral slices.

Perfusion data analysis

The level of agreement between sequences was evaluated by correlating the individual whole-brain mean CBF values. The reliability of the measurements across sequences was assessed by computing the within-subject coefficient of variation (wsCV) (24). This was achieved by first computing the CV for each subject as the ratio of the standard deviation to

the mean of the two repeated measurements. The wsCV was then calculated as the root mean square of the individual CVs.

The acquired perfusion maps were compared by evaluating the spatial and temporal perfusion signal-to-noise ratio (SNR) and the GM-to-WM CBF contrast ratio. The *spatial perfusion SNR* was computed as the ratio between the whole brain mean perfusion signal, $\mu_{perfusion}$, and the background noise level, σ_{noise} (Eq. 1). The background noise level was estimated by manually drawing two spherical Regions-Of-Interest (ROI) of 12 mm radius, in regions well outside the brain, and calculating the standard deviation of the signal within them. The absence of image artifacts within the background ROIs was assessed by examining the autocorrelation function of the noise signal. The noise SD was compensated for averaging ($N_{averages}$ = number of averages) and magnitude reconstruction (25).

$$SNR = \frac{1}{\frac{\sqrt{N_{averages}}}{0.655}} \cdot \frac{\mu_{perfusion}}{\sigma_{noise}} \quad [1]$$

The *temporal perfusion SNR* represents the stability of the perfusion signal over time. It was computed as the mean of the whole-brain perfusion signal in the time series, divided by its temporal standard deviation.

The *GM-to-WM CBF contrast ratio* was estimated as the ratio between the mean GM and WM CBF values.

Statistical differences in these parameters between the sequences were assessed by means of paired t-tests, and corrected for multiple comparisons using Bonferroni correction.

Point spread function simulations

The effective voxel size directly affects the image SNR, and is dependent on the readout parameters, particularly on the effective TE and readout length. Therefore, to assess the impact of each readout on the effective resolution, the PSF of each sequence was simulated.

First, the time evolution of the vascular signal was simulated for both 3D GRASE and 3D RARE Stack-Of-Spirals during the acquisition of a complete k_z plane. Next, the echo amplitudes in k_z direction were calculated. This allowed estimation of the PSFs of both sequences in-plane and in the slice direction, by Fourier transforming the simulated modulation transfer functions. For the simulations, it was assumed that the ASL signal emanates from the intravascular space (consistent with the single-compartment model, used for CBF quantification) and so the following relaxation times were employed: $T_{2,blood}$ = 186 ms (26), $T_2{}^*_{blood}$ = 73 ms (27). The amplitude of the excitation RF field (B_1) was assumed to be uniform over the imaging volume. A detailed description of the PSF simulation procedure has been included in Supplementary Material.

Evaluation of acoustic noise levels

Additionally, the level of acoustic noise generated by the two readouts was evaluated by computing the Sound Pressure Level (SPL) of the sound recorded during a 1-minute phantom scanning session with both readout sequences, in the absence of labeling.

RESULTS

In-vivo results

The group whole-brain mean CBF values measured with the two sequences under test were 57.8 ± 10.9 and 57.6 ± 11.7 ml/min/100g, for 3D RARE Stack-Of-Spirals and 3D GRASE, respectively (Table 1). At the individual level, the whole-brain mean CBF values obtained present a very high degree of agreement between sequences (Pearson's correlation coefficient $r = 0.95$, $p < 10^{-7}$). The within-subject coefficient of variation across sequences was 4.6% (95% confidence interval [3.8% - 5.4%]).

The 3D RARE Stack-Of-Spirals data presented an approximately 2-fold mean increase in spatial and temporal perfusion SNR over 3D GRASE (Spatial SNR: 8.5 ± 2.8 and 3.7 ± 1.4; Temporal SNR: 27.4 ± 12.5 and 15.6 ± 7.6, respectively). Additionally, GM-to-WM contrast ratio was slightly higher for 3D RARE Stack-Of-Spirals (2.9 ± 0.3 and 2.5 ± 0.3, respectively). The statistical tests revealed a significant difference in spatial and temporal SNR ($p < 10^{-7}$ and $p = 0.0045$, respectively), whereas no statistical significance was reached in GM-to-WM contrast ratio ($p = 0.17$). The noise autocorrelation functions measured within each background ROI can be found in Supplementary Material.

Figure 4 shows the mean perfusion maps of three representative subjects, scaled so that both 3D GRASE and 3D RARE Stack-Of-Spirals maps present the same mean perfusion level. The enhanced SNR of the 3D RARE Stack-Of-Spiral images can be observed as decreased noise level, which can be more easily seen in images with ×10 scaling (first column).

Figure 5 shows mean CBF maps obtained with both sequences on one representative subject, together with its corresponding T_1-weighted image. The in-plane resolution of the maps allows identifying fine anatomical structures, such as the different cortical gyri.

Susceptibility-induced off-resonance artifacts were observed in both 3D GRASE and 3D RARE Stack-Of-Spirals data (Fig. 6). In 3D RARE Stack-Of-Spirals, artifacts were evidenced as signal dropout in orbito-frontal and inferior-temporal regions, while in 3D GRASE artifacts were mainly observed in the form of signal distortion in orbito-frontal cortex and signal loss in inferior-temporal regions. A comprehensive analysis of eye-movement related artifacts in the two sequences, as well as the effect of PE direction on the image artifacts for 3D GRASE can be found in Supplementary Material.

PSF simulations

In the case of the 3D RARE Stack-Of-Spirals sequence, the simulated in-plane PSF is circularly symmetric (Fig. 7b), with a full-width-at-half-maximum ($FWHM_{XY}$) amplitude of 1.23 voxels in X and Y directions. The symmetry of this PSF is due to the radial symmetry

of the in-plane MTF (Fig. 7a), whereas leaving the far corners of the k-space unsampled contributes to the widening of the PSF.

The simulated 3D GRASE in-plane PSF is asymmetrical and broader in the Y direction, which corresponds to the phase encoding direction, where the $FWHM_Y$ in the Y direction was 1.02 voxels (Fig. 7b).

In the slice or Z direction, T_2 decay widens the PSF in both tested sequences. However, the shorter readout length in the 3D RARE Stack-Of-Spirals results in a $FWHM_Z = 1.57$ voxels, compared to a $FWHM_Z = 1.90$ voxels in the case of 3D GRASE. This is evidenced in Figure 4 as increased through-plane blurring in the coronal view of the 3D GRASE perfusion maps.

According to these results, the effective voxel size is larger than the nominal voxel size due to PSF blurring by a factor of 2.38 in the case of 3D RARE Stack-Of-Spirals and by a factor of 1.94 in the case of 3D GRASE.

Additionally, the simulations show an increase in the signal amplitude for the 3D RARE Stack-Of-Spirals sequence, due to its shorter TE_{Eff}, represented as a 25% increment in amplitude in the PSF with respect to 3D GRASE (Fig. 7c). Thus, according to the PSF simulations, the 3D RARE Stack-Of-Spirals is expected to yield a 1.5-fold increase in SNR of over 3D GRASE.

Acoustic noise levels

The analysis of acoustic noise generated by the readout sequences in the absence of labeling showed that the 3D RARE Stack-of-Spirals readout slightly lower intensity values. The calculated SPL of each readout type can be found in Supplementary Material.

DISCUSSION

The aim of this work was to implement and compare two ASL sequences optimized for whole-brain high-resolution perfusion imaging. To this end, we selected the most commonly used 3D segmented readout schemes, 3D GRASE and 3D RARE Stack-Of-Spirals, and combined them with pCASL labeling and background suppression. A direct comparison of these two readout approaches in their segmented configuration has not been previously reported. For both sequences, an in-plane 8-shot segmentation was implemented with a target resolution of $2\times2\times4mm^3$. For this multi-shot configuration, the number of shots was selected to minimize TE, and hence, readout time for both sequences. Furthermore, with a TR of 4s, an 8-shot segmentation yielded a total time per image of 32s, during which one must rely on the subject to remain still. Higher-order segmented schemes are usually not practical because of the increased probability of subject motion-related artifacts between shots (unless intra-session motion correction techniques are used). Other acquisition parameters that were independent of the in-plane k-space trajectories were kept the same for both sequences, in order to isolate the effect of the different in-plane trajectories.

In-vivo results and PSF simulations

The group whole-brain mean CBF values obtained are in the upper bound of the expected range of values for cohorts within this age range (28,29). This may be due to a slight underestimation of the calibration factor employed to calculate the CBF values. This value was measured in previous work (12), where an identical labeling pulse and BS scheme were tested. However, in the present work the labeling plane was carefully positioned for each subject, as perpendicular as possible to the brain feeding vessels, which likely led to an increase in the labeling efficiency.

The mean CBF values obtained with both sequences were highly correlated across subjects, with $r = 0.95$ ($p < 10e\text{-}7$) and with a wsCV under 5%, as expected since identical labeling parameters were used. The reproducibility of CBF measurements across sequences reinforces the notion that ASL MRI can measure a biological property of tissue that is independent of the imaging parameters and suggests that CBF measurements obtained with varying imaging schemes can be combined. However, differences between sequences were found in terms of perfusion SNR (both temporal and spatial) and GW-WM CBF contrast ratio, although the latter did not reach statistical significance. SNR is a particularly important parameter for clinical applications of ASL where interpretations are being made on individual datasets. Spatial perfusion SNR was increased in 3D RARE Stack-Of-Spirals with respect to 3D GRASE by approximately a factor of 2, partially explained by the larger effective voxel size and increased signal amplitude, according to the PSF simulations. Similarly, temporal SNR was also increased for 3D RARE Stack-Of-Spirals, likely as a result of the higher stability of the perfusion signal over time due to the high oversampling of the central k-space, which contributes to increasing the sequence robustness against motion artifacts (30) and therefore reduces temporal signal variations caused by these effects. Although spatial SNR measures may vary according to the location of the ROI used to estimate noise levels, the signal autocorrelation functions within the chosen background ROIs indicate that these were free of image artifacts. Temporal SNR, on the other hand, is independent of ROI location. However, due to the limited number of time-points in the segmented acquisitions (only six perfusion pairs were acquired) the variability of the temporal SNR values was higher than that of the spatial SNR.

According to the simulated PSFs, the effective voxel size was larger than the nominal voxel size for both sequences. 3D RARE Stack-Of-Spirals presented a larger in-plane effective voxel size than 3D GRASE. This stems from the nature of the spiral readout, in which the far-corners of every k_z plane are left unsampled, widening the in-plane PSF uniformly in all directions, and therefore increasing the in-plane effective voxel size. Conversely, the effective voxel size in the slice direction was smaller in 3D RARE Stack-Of-Spirals than in 3D GRASE. This is due to the time-efficiency of the former: in addition to having shorter TE_{Eff}, 3D RARE Stack-Of-Spirals requires significantly less time to sample each k-space segment, thus suffering from less T_2 decay. Overall, the PSF simulations showed that 3D RARE Stack-Of-Spirals had a 20% larger effective voxel volume than 3D GRASE. With the spatial SNR being proportional to voxel size, this effect contributes to a proportional rise in image SNR, at the expense of a loss in image resolution.

Additionally, it was observed that the 3D RARE Stack-Of-Spirals presented a 25% higher signal level compared to 3D GRASE, arising from the shorter effective TE. Both effects together explain a 1.5-fold increase in SNR in 3D RARE Stack-Of-Spirals with respect to 3D GRASE. The in-vivo measurements however showed a 2-fold increase in SNR. The difference could be explained by other factors affecting spatial SNR, as discussed below.

Other factors affecting spatial SNR

Receiver BW—The receiver BW influences SNR, since noise variance is directly proportional to BW. Decreasing BW while keeping all other parameters constant would increase SNR, however in practice, decreasing BW increases TE_{Eff} and total readout time, thus decreasing SNR and leading to more severe T_2 decay that affects image resolution. For this reason, the highest possible BW was selected for 3D GRASE in order to achieve minimum TE and shorter readout time. The chosen BW was limited by the maximum gradient amplitude available on the scanner ($BW_{3D\ GRASE}$ = 2298 Hz/px, while $BW_{3D\ RARE}$ = 3125 Hz/px). The higher BW of the spiral readout would translate into higher noise variance, and thus, reduced SNR.

FOV—A typical feature of 3D GRASE sequences, such as the one employed here, is the use of rectangular FOVs instead of square FOVs. In 3D GRASE, decreasing the FOV in the PE direction reduces the amount of lines to acquire and therefore saves readout time, which has a positive impact on the image resolution because it decreases T_2 decay. This approach could have the effect of reducing SNR, since the signal is proportional to the square root of the number of phase-encoding lines. In 3D RARE Stack-Of-Spirals the FOV is circular, thus SNR is also reduced compared to square FOV sampling. However, in practice, since the signal is heavily concentrated around the center of k-space, the highest spatial frequency components contain mainly noise, thus diminishing the effect of the reduced sampling on the SNR.

T_2 decay—The impact of T_2 decay on the image resolution as a function of readout time, and therefore on the perfusion SNR has been characterized by simulating the PSFs of both sequences. Besides this effect, T_2 decay can also be a source of additional SNR loss in the presence of long readout times. Due to the increased length of the readout in the 3D GRASE sequence, the level of the simulated perfusion signal by the end of the readout is ~8% of the originally excited signal, compared to the 16% level that is present in 3D RARE Stack-Of-Spirals. Thus, it is likely that by the time the outer part of the k-space is sampled in 3D GRASE, the perfusion signal has decreased below the coil sensitivity level, becoming undetectable, and therefore the contribution of those points to the reconstructed maps is limited to noise.

Spiral and Cartesian sampling—In Cartesian sampling, for a given BW the noise power (i.e. noise variance) is constant for all frequencies (Fig. 8a). However, in spiral imaging noise is heavily filtered due to oversampling, which is specially pronounced at the lower frequencies (Fig. 8b). In spiral imaging, non-uniform data are interpolated to fit a uniformly-distributed grid, similar to the one acquired in the Cartesian case (31). This process correctly estimates the gridded signal, but it also modifies the noise properties, due

to the fact that the noise amplitude, rather than the noise power, is being weighted in this process (32,33).

Regridding of spiral data is typically performed with an oversampling factor (OS) of 2, that is, non-uniform sampled data are usually regridded onto a grid of size 2N×2N, where N is the desired image matrix size (34). This doubles the FOV in each dimension, with the desired image located at the central N×N voxels and aliasing noise due to gridding constrained to the outer portion of the image.

The noise variance of each regridded point will be a function of sampling BW and the square sum of the interpolation coefficients, which depend on the selected OS (32,35). As illustrated in Fig. 2, the oversampling is more pronounced around the central frequencies than in the outer part of k-space. This can induce coherent or colored noise in the reconstructed images, since lower frequencies will have higher SNR than higher frequencies (35,36).

Provided the noise autocorrelation function in the spiral case is still approximately white, and taking into account the OS factor, for this particular spiral design the noise variance per voxel in the image after regridding and Fourier transforming is on average 0.9 times the variance of a uniform sampling scheme with same BW and matrix size.

It is additionally worth noting that the oversampling around the center of k-space leads to a significant drop in noise level for these frequencies (Fig. 8b). Since the majority of the signal is typically concentrated within the lower frequency range, this can result in an apparent increase of overall SNR in the image domain, but it could also lead to a loss of SNR around fine detailed structures.

Finally, it has been demonstrated that oversampling the center of k-space increases the robustness of the sequence against motion artifacts (30,37), which are typically low-frequency driven. This is particularly relevant in segmented acquisitions, where only a fraction of the k-space is acquired per TR. In the 3D RARE Stack-Of-Spirals acquisition, the center of k-space is not only greatly oversampled but also acquired repeatedly at every shot. This can positively affect the SNR of the reconstructed images by reducing motion-related noise.

Comparison with previous findings

The results found in this work are in agreement with previous studies (38-40), in which SNR increases were also reported when comparing either interleaved or segmented spiral-based sequences with segmented Cartesian-based sequences. In (38), 3D coronary MRA images were acquired using a Cartesian 10-segment k-space gradient echo sequence and a highly segmented 3D Stack-Of-Spirals sequence with two variants: single-interleaf per shot acquisition, and two-interleaf per shot acquisition. SNR increases of 2.6-fold and 1.8-fold were found with respect to the Cartesian sampling, respectively. In (39), PASL images obtained with single-shot 2D EPI, single-shot 2D spiral and two-segment 2D spiral were compared, and found SNR increases up to 195% in the tagged/control images and 62% in the spiral perfusion-weighted images.

In previous work (12), single-shot versions of the two sequences tested here were also compared. However, only a slight SNR difference was found. Although the absolute SNR values obtained are not directly comparable with the present work due to differences in the acquisition parameters (voxel size, number of partitions acquired, etc.), the discrepancy with the results presented here can be explained by differences in readout design between the two versions. In the single-shot sequence, a spiral scheme with a two consecutive interleaved acquisition was employed, so there was no effective TE reduction with respect to the single-shot GRASE sequence. The total readout duration was also comparable between sequences, thus eliminating the through-plane resolution differences and the spiral signal gain with respect to 3D GRASE. Furthermore, 160° refocusing RF pulses were chosen for the spiral scheme to decrease the SAR level, which slightly decreased the amplitude of the measured signal. Most importantly, BW for the single-shot spiral was 6250Hz/px compared to 2790Hz/px in 3D GRASE, thus increasing the noise per voxel in the image in the 3D RARE Stack-Of-Spirals sequence.

Sensitivity to off-resonance artifacts

Susceptibility-induced off-resonance artifacts were present in the images, although greatly reduced as compared to single-shot acquisitions (39,41,42), due to the shorter effective TE and readout times employed. 3D RARE Stack-Of-Spirals images showed slightly higher sensitivity to off-resonance artifacts, due to the fact that the k-space center was not sampled during the spin-echo time, presenting signal dropout in orbito-frontal regions and signal loss in inferior-temporal lobe regions. In 3D GRASE signal distortions were observed in orbito-frontal regions, due to the displacement of the signal in the PE direction caused by the susceptibility background gradients (42) while inferior-temporal lobe regions suffer from signal loss, although less severe than in 3D RARE Stack of Spirals.

Future work should include field-inhomogeneity correction strategies to compensate for the spurious phase accumulation during sampling (43-45). Parallel acquisition strategies could help further reduce the readout duration, hence decreasing the sensitivity to susceptibility artifacts (46), although with an associated penalty in SNR. Additionally, the use of a low flip angle refocusing train as means of decreasing through-plane blurring could be explored. However its impact on echo signal amplitude and SNR needs to be evaluated. Alternatively, more elaborated segmentation strategies combining both in-plane and through-plane segmentation could be investigated, as a means to further reduce the acquisition time per shot (47), evaluating their effect on TE and SNR.

In conclusion, the combination of pCASL, 3D segmented readouts and BS provides high-SNR high-resolution ASL acquisitions of the whole brain. Although both 3D GRASE and 3D RARE Stack-Of-Spirals produced excellent image quality, the 3D RARE Stack-Of-Spirals readout yielded a 2-fold increase in SNR and decreased through-plane blurring due to its inherent oversampling of the central k-space, its reduced effective TE and shorter total readout time, at the expense of a 20% increase in the effective voxel volume.

Supplementary Material

Refer to Web version on PubMed Central for supplementary material.

Acknowledgments

We are thankful to Dr. David Alsop for his help with the implementation of the 3D RARE Stack-Of-Spirals sequence and BS optimization. We also thank Drs. Josef Pfeuffer and Tiejun Zhao from Siemens for their help with the spiral readout and online reconstruction programming. We thank Drs. David Feinberg and Matthias Guenther for sharing the original 3D GRASE source code. We also thank Dr. Fernández-González for his help in the analysis of the acoustic characteristics of the two readouts.

This work was supported by the Spanish Ministry of Science and Innovation (grants SAF2011-29344 and RYC-2010-07161), the COST Action BM1103 and the National Institutes of Health (grants R01MH080729 and RR02305).

References

1. Detre JA, Leigh JS, Williams DS, Koretsky AP. Perfusion imaging. Magn Reson Med. 1992; 23(1): 37–45. [PubMed: 1734182]
2. Williams DS, Detre JA, Leigh JS, Koretsky AP. Magnetic resonance imaging of perfusion using spin inversion of arterial water. Proc Natl Acad Sci U S A. 1992; 89(1):212–216. [PubMed: 1729691]
3. Detre JA, Rao H, Wang DJ, Chen YF, Wang Z. Applications of arterial spin labeled MRI in the brain. J Magn Reson Imaging. 2012; 35(5):1026–1037. [PubMed: 22246782]
4. Raichle ME. Behind the scenes of functional brain imaging: a historical and physiological perspective. Proc Natl Acad Sci U S A. 1998; 95(3):765–772. [PubMed: 9448239]
5. Aguirre GK, Detre JA, Wang J. Perfusion fMRI for functional neuroimaging. Int Rev Neurobiol. 2005; 66:213–236. [PubMed: 16387205]
6. Dai W, Garcia D, de Bazelaire C, Alsop DC. Continuous flow-driven inversion for arterial spin labeling using pulsed radio frequency and gradient fields. Magn Reson Med. 2008; 60(6):1488–1497. [PubMed: 19025913]
7. Fernandez-Seara MA, Edlow BL, Hoang A, Wang J, Feinberg DA, Detre JA. Minimizing acquisition time of arterial spin labeling at 3T. Magn Reson Med. 2008; 59(6):1467–1471. [PubMed: 18506806]
8. Gunther M, Oshio K, Feinberg DA. Single-shot 3D imaging techniques improve arterial spin labeling perfusion measurements. Magn Reson Med. 2005; 54(2):491–498. [PubMed: 16032686]
9. Nielsen JF, Hernandez-Garcia L. Functional perfusion imaging using pseudocontinuous arterial spin labeling with low-flip-angle segmented 3D spiral readouts. Magn Reson Med. 2013; 69(2):382–390. [PubMed: 22488451]
10. Garcia DM, Duhamel G, Alsop DC. Efficiency of inversion pulses for background suppressed arterial spin labeling. Magn Reson Med. 2005; 54(2):366–372. [PubMed: 16032674]
11. Ye FQ, Frank JA, Weinberger DR, McLaughlin AC. Noise reduction in 3D perfusion imaging by attenuating the static signal in arterial spin tagging (ASSIST). Magn Reson Med. 2000; 44(1):92–100. [PubMed: 10893526]
12. Vidorreta M, Wang Z, Rodriguez I, Pastor MA, Detre JA, Fernandez-Seara MA. Comparison of 2D and 3D single-shot ASL perfusion fMRI sequences. Neuroimage. 2012; 66C:662–671. [PubMed: 23142069]
13. Talagala SL, Ye FQ, Ledden PJ, Chesnick S. Whole-brain 3D perfusion MRI at 3.0 T using CASL with a separate labeling coil. Magn Reson Med. 2004; 52(1):131–140. [PubMed: 15236376]
14. Feinberg, DA.; Ramanna, S.; Guenther, M. Evaluation of new ASL 3D GRASE sequences using Parallel Imaging, Segmented and Interleaved k-space at 3T with 12- and 32-channel coils. Proceedings of the 17th Annual Meeting of ISMRM; Honolulu, Hawaii, USA. 2009.
15. Xu G, Rowley HA, Wu G, Alsop DC, Shankaranarayanan A, Dowling M, Christian BT, Oakes TR, Johnson SC. Reliability and precision of pseudo-continuous arterial spin labeling perfusion MRI on 3.0 T and comparison with 15O-water PET in elderly subjects at risk for Alzheimer's disease. NMR Biomed. 2010; 23(3):286–293. [PubMed: 19953503]

16. Ordidge RJ, Wylezinska M, Hugg JW, Butterworth E, Franconi F. Frequency offset corrected inversion (FOCI) pulses for use in localized spectroscopy. Magn Reson Med. 1996; 36(4):562–566. [PubMed: 8892208]
17. King KF, Foo TK, Crawford CR. Optimized gradient waveforms for spiral scanning. Magn Reson Med. 1995; 34(2):156–160. [PubMed: 7476073]
18. Robison RK, Devaraj A, Pipe JG. Fast, simple gradient delay estimation for spiral MRI. Magn Reson Med. 2010; 63(6):1683–1690. [PubMed: 20512872]
19. Nuttall AH. Some windows with very good sidelobe behavior. IEEE Trans Acoust Speech Signal Processing. 1981; 29(1):84–91.
20. Frigo M, Johnson SG. The design and implementation of FFTW3. Proc IEEE. 2005; 93(2):216–231.
21. Feinberg DA, Oshio K. Gradient-Echo Shifting in Fast MRI Techniques (GRASE Imaging) for Correction of Field Inhomogeneity Errors and Chemical Shift. Journal of Magnetic Resonance. 1992; 97:177–183.
22. Wang J, Zhang Y, Wolf RL, Roc AC, Alsop DC, Detre JA. Amplitude-modulated continuous arterial spin-labeling 3.0-T perfusion MR imaging with a single coil: feasibility study. Radiology. 2005; 235(1):218–228. [PubMed: 15716390]
23. van Gelderen P, de Zwart JA, Duyn JH. Pittfalls of MRI measurement of white matter perfusion based on arterial spin labeling. Magn Reson Med. 2008; 59(4):788–795. [PubMed: 18383289]
24. Bland JM, Altman DG. Statistics notes: measurement error. Brit Med J. 1996; 312(7047):1654. [PubMed: 8664723]
25. Kaufman L, Kramer DM, Crooks LE, Ortendahl DA. Measuring signal-to-noise ratios in MR imaging. Radiology. 1989; 173(1):265–267. [PubMed: 2781018]
26. Chen JJ, Pike GB. Human whole blood T2 relaxometry at 3 Tesla. Magn Reson Med. 2009; 61(2): 249–254. [PubMed: 19165880]
27. Zhao JM, Clingman CS, Narvainen MJ, Kauppinen RA, van Zijl PC. Oxygenation and hematocrit dependence of transverse relaxation rates of blood at 3T. Magn Reson Med. 2007; 58(3):592–597. [PubMed: 17763354]
28. Lassen NA. Normal average value of cerebral blood flow in younger adults is 50 ml/100 g/min. J Cereb Blood Flow Metab. 1985; 5(3):347–349. [PubMed: 4030914]
29. Leenders KL, Perani D, Lammertsma AA, Heather JD, Buckingham P, Healy MJ, Gibbs JM, Wise RJ, Hatazawa J, Herold S, et al. Cerebral blood flow, blood volume and oxygen utilization. Normal values and effect of age. Brain. 1990; 113(Pt1):27–47. [PubMed: 2302536]
30. Liao JR, Pauly JM, Brosnan TJ, Pelc NJ. Reduction of motion artifacts in cine MRI using variable-density spiral trajectories. Magn Reson Med. 1997; 37(4):569–575. [PubMed: 9094079]
31. O'Sullivan JD. A fast sinc function gridding algorithm for fourier inversion in computer tomography. IEEE Trans Med Imaging. 1985; 4(4):200–207. [PubMed: 18243972]
32. Rosenfeld D. New approach to gridding using regularization and estimation theory. Magn Reson Med. 2002; 48(1):193–202. [PubMed: 12111946]
33. Callaghan, PT. Principles of Nuclear Magnetic Resonance Microscopy. Oxford: Oxford University Press Inc.; 1993. High-Resolution k-Space Imaging; p. 173-226.
34. Jackson JI, Meyer CH, Nishimura DG, Macovski A. Selection of a convolution function for Fourier inversion using gridding. IEEE Trans Med Imaging. 1991; 10(3):473–478. [PubMed: 18222850]
35. Newbould, RD.; Liu, C.; Bammer, R. Colored Noise and Effective Resolution: Data considerations for non-uniform k-space sampling reconstructions. Proceedings of the 14th Annual Meeting of ISMRM; Seattle, Washington, USA. 2006.
36. Haacke, EM.; Brown, RW.; Thompson, MR.; Venkatesan, R. Magnetic Resonance Imaging - Physical Principles and Sequence Design. New York: John Wiley & Sons Inc.; 1999. Signal, Contrast and Noise; p. 331-380.
37. Glover GH. Spiral imaging in fMRI. Neuroimage. 2012; 62(2):706–712. [PubMed: 22036995]

38. Bornert P, Stuber M, Botnar RM, Kissinger KV, Koken P, Spuentrup E, Manning WJ. Direct comparison of 3D spiral vs. Cartesian gradient-echo coronary magnetic resonance angiography. Magn Reson Med. 2001; 46(4):789–794. [PubMed: 11590656]

39. Lehmann, B.; Zhao, T.; Pfeuffer, J. Benefits of spiral imaging for Arterial Spin Labeling as compared to EPI. Proceedings of the 21th Annual Meeting of ISMRM; Salt Lake City, Utah, USA. 2013.

40. Taylor AM, Keegan J, Jhooti P, Gatehouse PD, Firmin DN, Pennell DJ. A comparison between segmented k-space FLASH and interleaved spiral MR coronary angiography sequences. J Magn Reson Imaging. 2000; 11(4):394–400. [PubMed: 10767068]

41. Ramanna S, Feinberg DA. Single-shot 3D GRASE with cylindrical k-space trajectories. Magn Reson Med. 2008; 60(4):976–980. [PubMed: 18816819]

42. Fernandez-Seara MA, Wang Z, Wang J, Rao HY, Guenther M, Feinberg DA, Detre JA. Continuous arterial spin labeling perfusion measurements using single shot 3D GRASE at 3 T. Magn Reson Med. 2005; 54(5):1241–1247. [PubMed: 16193469]

43. Cheng JY, Santos JM, Pauly JM. Fast concomitant gradient field and field inhomogeneity correction for spiral cardiac imaging. Magn Reson Med. 2011; 66(2):390–401. [PubMed: 21384423]

44. Noll DC, Meyer CH, Pauly JM, Nishimura DG, Macovski A. A homogeneity correction method for magnetic resonance imaging with time-varying gradients. IEEE Trans Med Imaging. 1991; 10(4):629–637. [PubMed: 18222870]

45. Man LC, Pauly JM, Macovski A. Multifrequency interpolation for fast off-resonance correction. Magn Reson Med. 1997; 37(5):785–792. [PubMed: 9126954]

46. Weiger M, Pruessmann KP, Osterbauer R, Bornert P, Boesiger P, Jezzard P. Sensitivity-encoded single-shot spiral imaging for reduced susceptibility artifacts in BOLD fMRI. Magn Reson Med. 2002; 48(5):860–866. [PubMed: 12418001]

47. Balteau, E.; Vidorreta, M.; Fernández-Seara, MA.; De Vita, E.; Thomas, DL. New segmentation scheme for improved point spread function in multi-shot 3D-GRASE pCASL. Proceedings of the 30th Annual Meeting of ESMRMB; Toulouse, France. 2013.

LIST OF ABBREVIATIONS USED

ASL	Arterial Spin Labeling
BS	Background Suppression
BW	Bandwidth
CASL	Continuous Arterial Spin Labeling
CBF	Cerebral Blood Flow
FOV	Field-Of-View
FWHM	Full Width at Half Maximum
GM	Grey Matter
GRASE	GRadient And Spin Echo
MPRAGE	Magnetization Prepared RApid Gradient Echo
OS	Oversampling Factor
pCASL	Pseudo-Continuous Arterial Spin Labeling
PE	Phase Encoding
PF	Partial Fourier

PLD	Post-Labeling Delay
PSF	Point Spread Function
RARE	Rapid Acquisition with Relaxation Enhancement
RF	Radio-Frequency
ROI	Region-Of-Interest
SD	Standard Deviation
SNR	Signal-to-Noise Ratio
SPL	Sound Pressure Level
TI	Inversion Time
TOF	Time-Of-Flight
WM	White Matter
wsCV	within-subject Coefficient of Variation

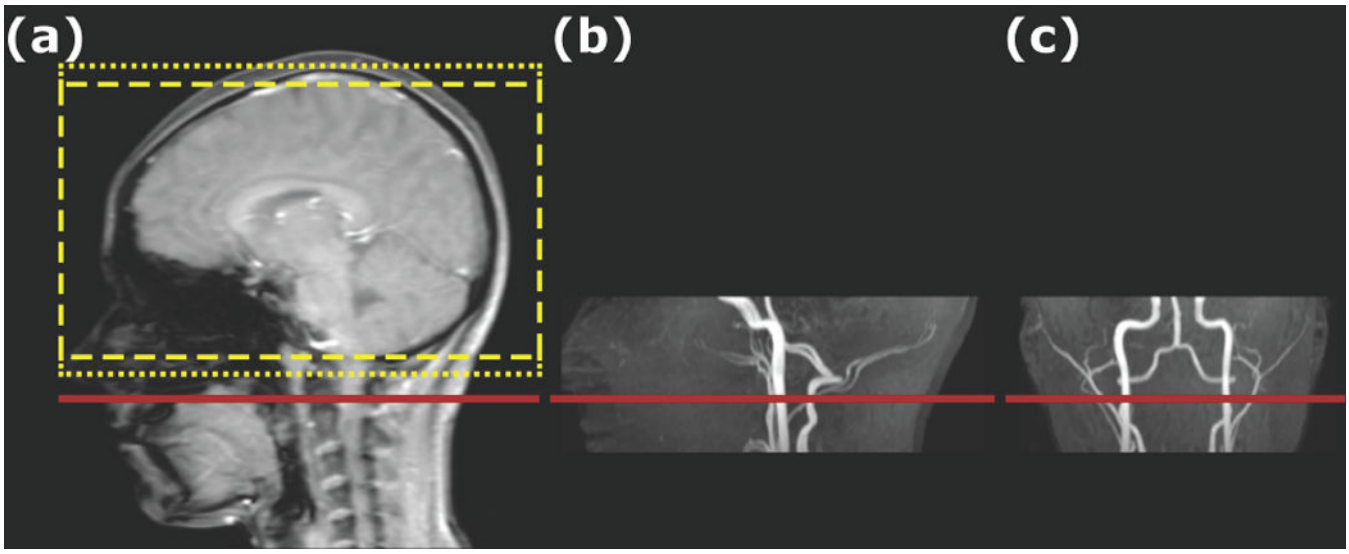

Figure 1.

Positioning of the labeling plane (continuous red line) and ASL imaging slab (dashed yellow line, oversampled area denoted with dotted line) in one of the subjects: **(a)** Sagittal scout image; **(b)** Sagittal angiogram; **(c)** Coronal angiogram.

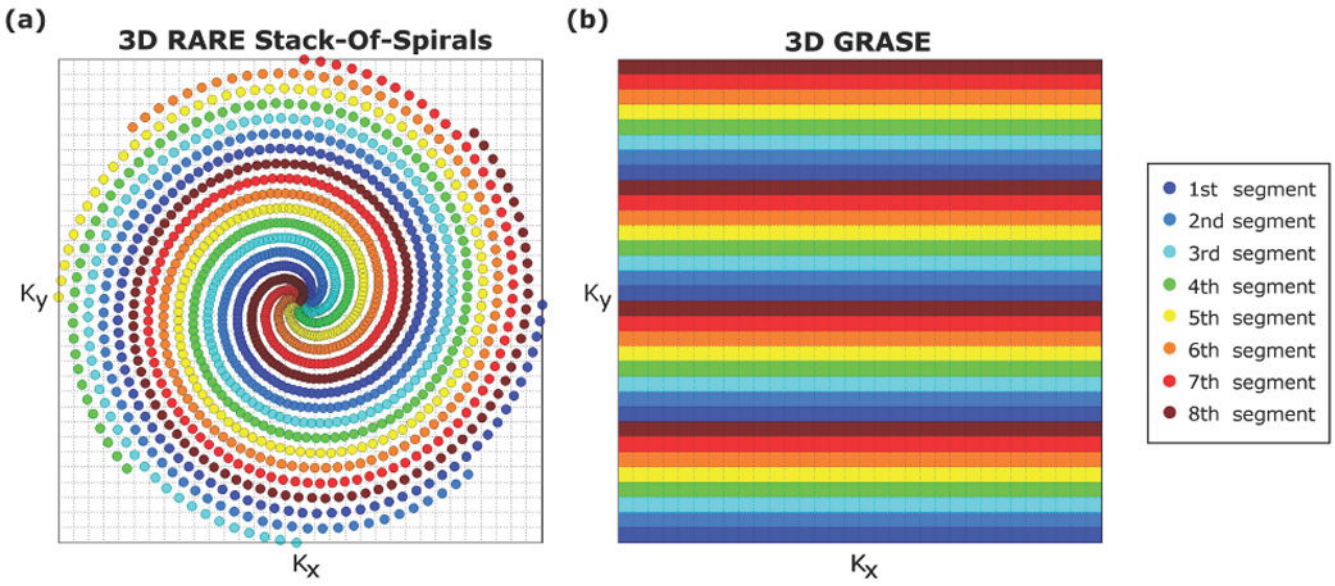

Figure 2.

Illustration of the 8-shot in-plane segmentation scheme of **(a)** 3D RARE Stack-Of-Spirals and **(b)** 3D GRASE. The former divides the k-space plane into 8 spiral interleaves, while the latter divides it into 8 segments, reading one in every 8 lines per shot. *Here segmentation is shown on a 32×32 voxel grid, for illustration purposes*.

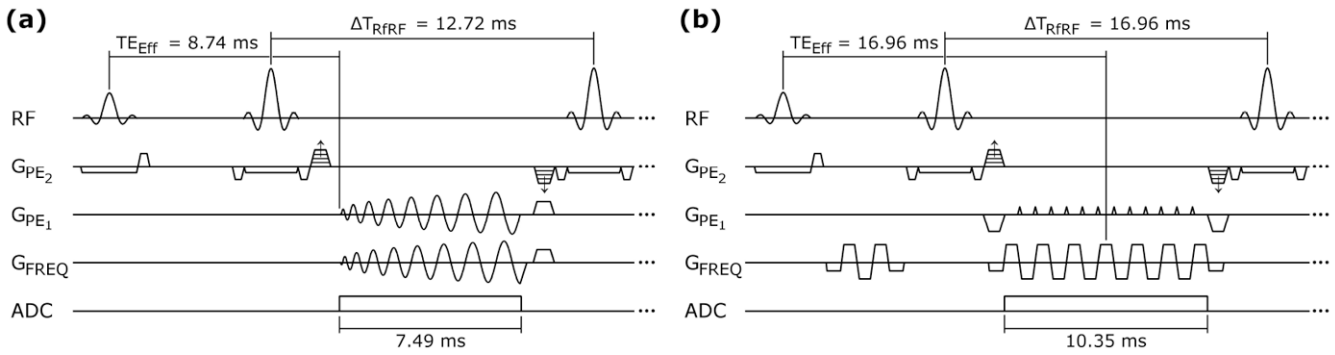

Figure 3.

Sequence diagram of **(a)** 3D RARE Stack-Of-Spirals readout, and **(b)** 3D GRASE readout. Displayed parameters are: effective echo time (TE_{Eff}), time between 180° refocusing RF pulses (ΔT_{RfRF}) and readout time per k_z plane. *Here in-plane gradient waveforms are drawn schematically for illustration purposes and do not show the full length echo trains.*

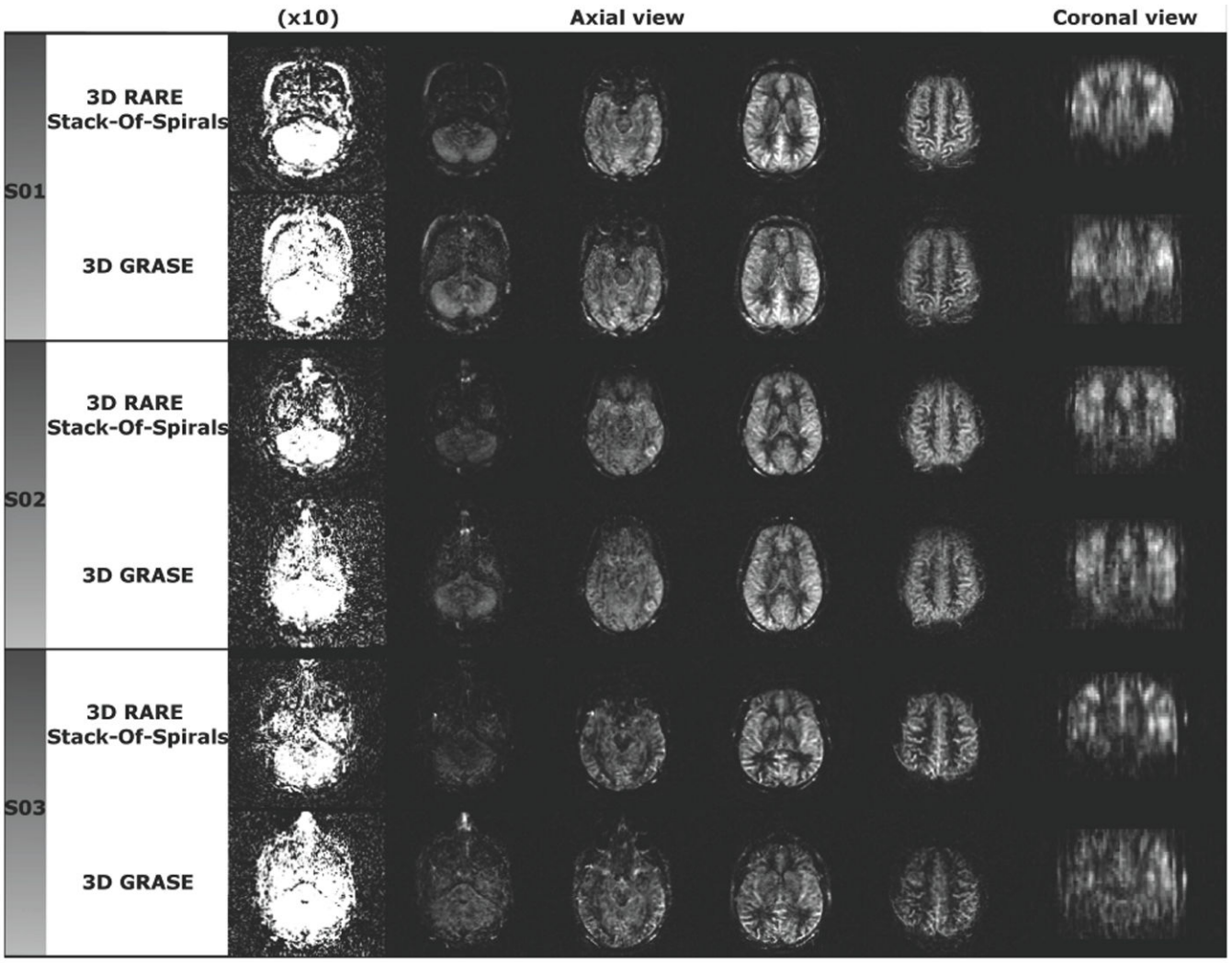

Figure 4.

Mean perfusion maps acquired with 3D RARE Stack-Of-Spirals and 3D GRASE on three representative subjects, scaled to the same mean perfusion signal level. Four axial slices and one coronal view are depicted for each map. The scale of the lower axial slice from each map has been amplified by a factor of 10 to facilitate the visual inspection of noise in the maps (first column). Note the increased noise level in the 3D GRASE maps, as well as the enhanced GM-to-WM contrast ratio and decreased through-plane blurring in the 3D RARE Stack-Of-Spirals maps.

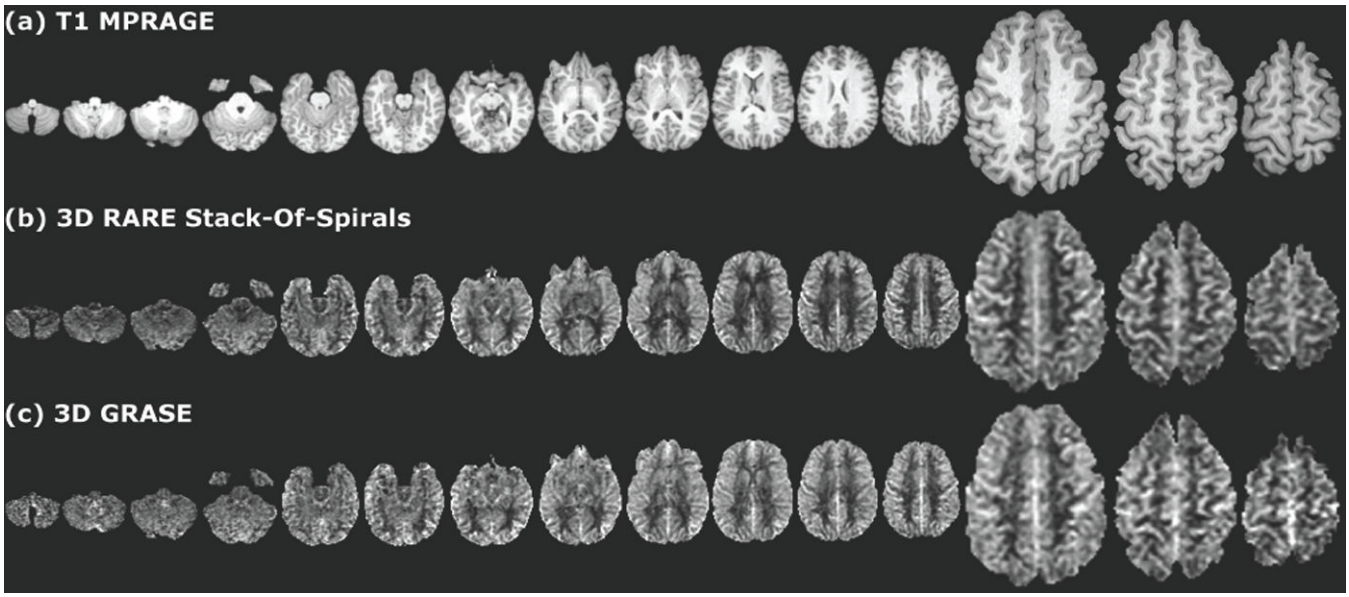

Figure 5.

(a) T_1-weighted anatomical dataset, and mean CBF maps of one representative subject, obtained with **(b)** 3D RARE Stack-Of-Spirals and **(c)** 3D GRASE. The last three axial slices have been enlarged to facilitate the inspection of anatomical detail in the maps. The scale of the CBF maps is [0 100] ml/min/100g of tissue.

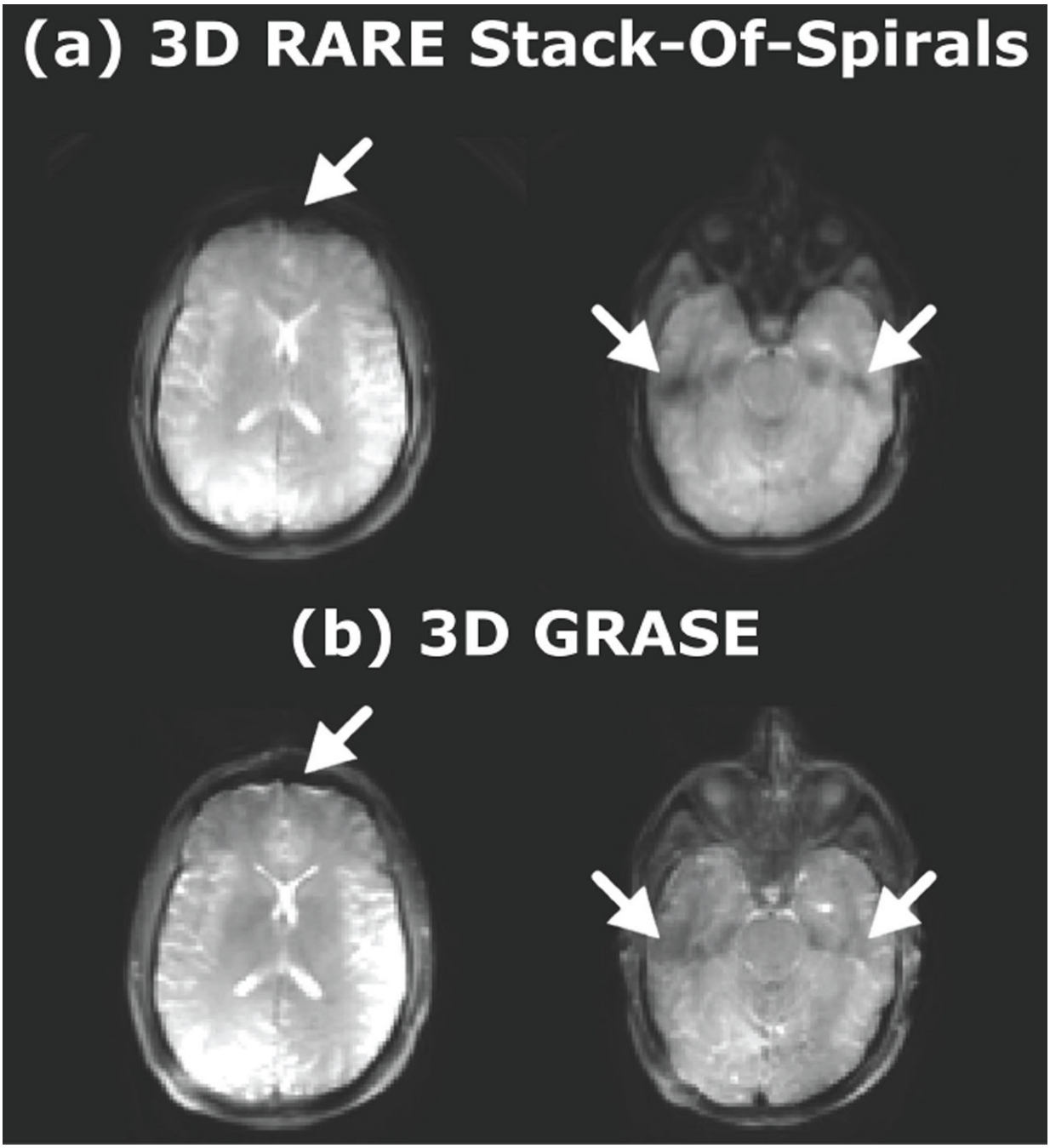

Figure 6.

Two slices of the control images obtained with **(a)** 3D RARE Stack-Of-Spirals, and **(b)** 3D GRASE on a representative subject. White arrows point to regions where susceptibility-induced off-resonance artifacts were observed.

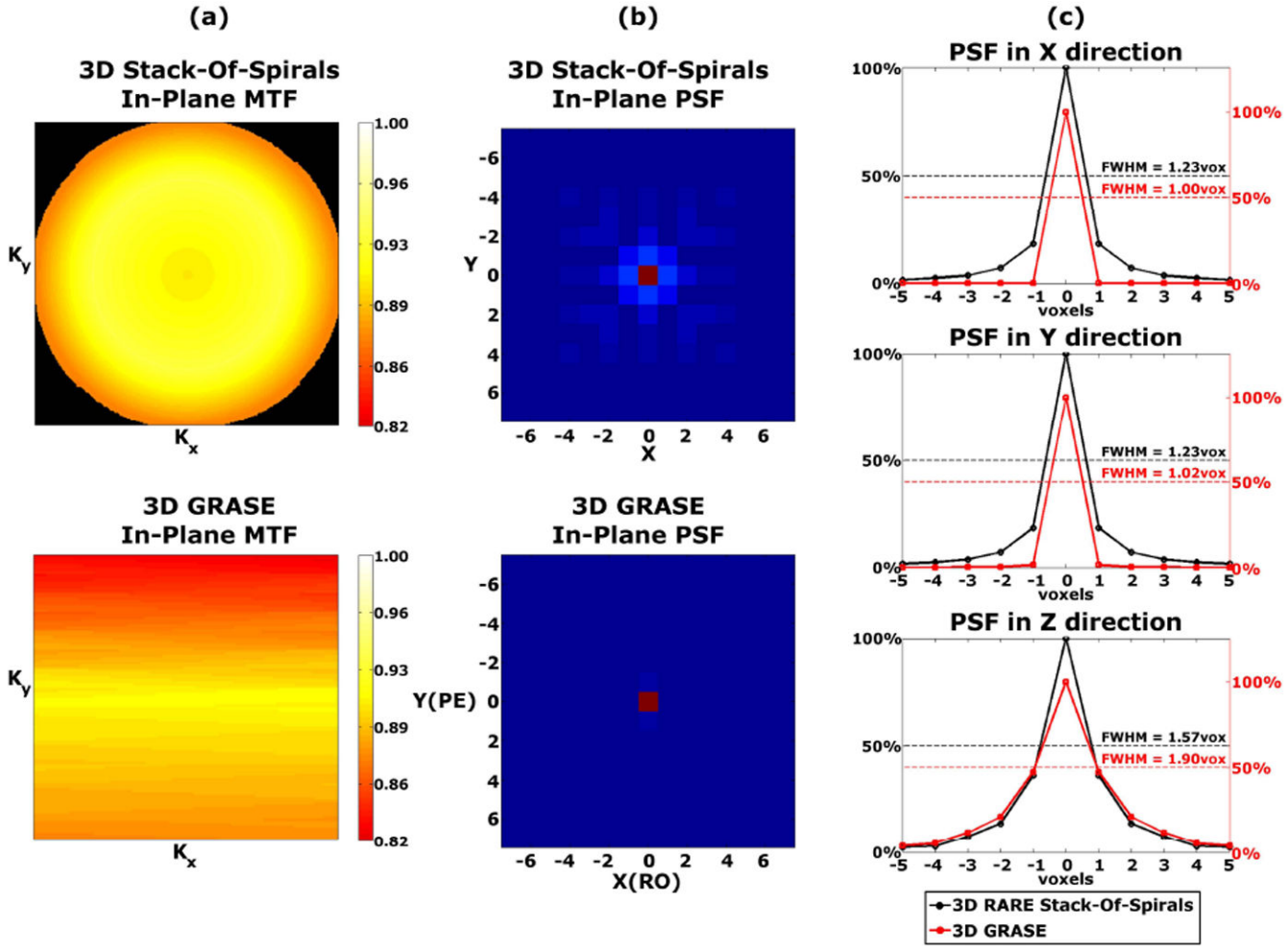

Figure 7.

(a) In-plane simulated modulation transfer functions (MTF) and **(b)** point spread functions (PSF) for the tested sequences, 3D RARE Stack-Of-Spirals and 3D GRASE. **(c)** Comparison of PSFs between the two sequences in X, Y and Z directions. The Full-Width-at-Half-Maximum (FWHM) of the PSFs is indicated.

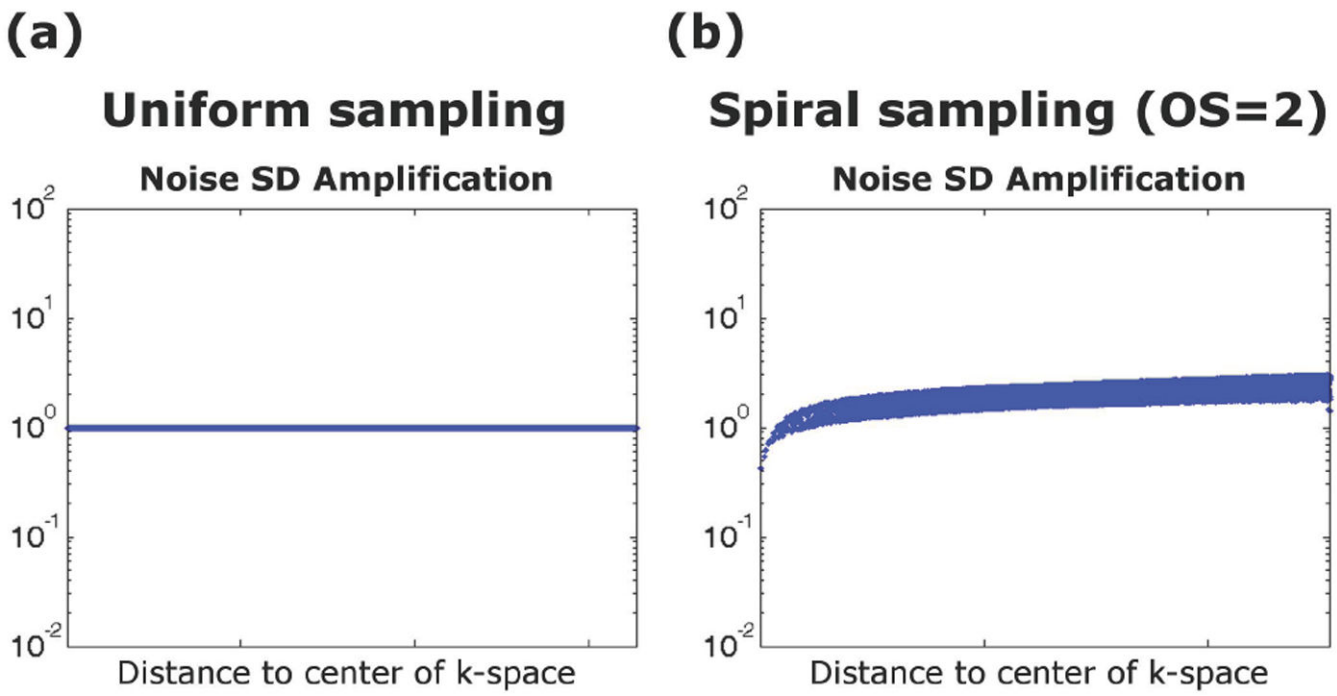

Figure 8.

Noise distribution in uniform sampling **(a)** and in spiral sampling with an oversampling factor (OS) of 2 **(b)**, depicting the amplification of the noise standard deviation (SD) in frequency space with respect to the noise level in a uniform sampling scheme with same BW and matrix size.

Table 1

In-vivo perfusion results for 3D RARE Stack-Of-Spirals and 3D GRASE. *Group data are displayed as mean ± standard deviation.*

	Mean CBF			GM-WM CBF Contrast	Spatial Perfusion SNR	Temporal Perfusion SNR
	Global	GM	WM			
3D RARE Stack-Of-Spirals	57.8 ± 10.9	75.4 ± 13.0	26.5 ± 6.4	2.9 ± 0.3	8.5 ± 2.8	27.4 ± 12.5
3D GRASE	57.6 ± 11.7	73.2 ± 14.5	30.1 ± 7.7	2.5 ± 0.3	3.7 ± 1.4	15.6 ± 7.6